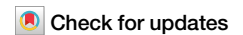


<https://doi.org/10.1038/s42005-024-01646-1>

Rheology of a crowd: from faster-is-slower to shear thickening

Dariel Hernández-Delfin¹ ✉, Ander García^{1,2} & Marco Ellero^{1,3,4} ✉

The evacuation speed of pedestrians through bottlenecks usually leads to the faster-is-slower (FIS) phenomenon, which relies on frictional clogging and clusters' size. However, less attention is given in literature to the rheology of pedestrian crowds and the forces ruling their dynamics. Here, we establish a link between the faster-is-slower phenomenon (FIS) in pedestrian crowds and the shear-thickening rheological behavior of (non)Brownian suspensions. We analyze pedestrian room egress through particle-based simulations using the Social Force Model, revealing an S-shaped shear rate dependency characteristic of discontinuous shear thickening (DST). At the same time, the crowd flow viscosity near the exit exhibits a steep increase coinciding with FIS occurrence, establishing a correlation between FIS and shear thickening. Our results prove that crowd evacuations are governed by two distinct critical jamming densities, one frictional and another frictionless, and that contact forces alone cannot lead to FIS, but social force interactions are necessary to avoid contacts at low desired speeds. Our results point at the suitability of (non)Brownian suspensions as models that provide an original rheological perspective to pedestrian dynamics.

The complex dynamics underlying pedestrian crowd evacuation have captured the attention of researchers in different study areas. Understanding the nature of the behavior of pedestrians plays an essential role in predicting and avoiding disasters related to crowd systems. Based on the information gathered through investigations, substantial advances may be devised in terms of the design of facilities and safety procedures to prevent catastrophic scenarios and optimize the movement of pedestrian crowds. Special relevance lies in systems where the pedestrian number in an area of interest is high, and the characteristics of the geometry change abruptly, e.g., bottlenecks^{1–5}. In this context, evacuation of pedestrian crowds is undoubtedly crucial due to the existent relationship with safety in view of preventing fatal accidents.

When pedestrian crowds evacuate through bottlenecks with certain competitiveness, the evacuation becomes faster as the competitiveness is higher until a critical point. From such point, the evacuation becomes slower despite the increasing competitiveness. Although this phenomenon is empirically well-known, it was not described until 2000, when Helbing et al.¹ obtained it through numerical simulations based on their social force model (SFM)⁶ and named it *faster-is-slower* (FIS). FIS has been confirmed in a number of experiments^{7–9} and numerical studies^{1,10}. In the context of the SFM, three distinct forces are considered, which are the desired force \mathbf{f}^d ,

frictionless repulsive long-range social force \mathbf{f}^s , and frictional contact force \mathbf{f}^c . \mathbf{f}^d exerts an acceleration on pedestrians with the end of changing their current velocity to the desired velocity $\mathbf{v}_i^0 = v_i^0 \mathbf{e}_i$, where v_i^0 is the desired speed. Here, \mathbf{e}_i is the direction an individual pedestrian i takes if it is isolated from other pedestrians or obstacles that might perturb its movement. In this way, the desired force of an individual pedestrian reads

$$\mathbf{f}_i^d = m_i \frac{\mathbf{v}_i^0 - \mathbf{v}_i}{\tau}, \quad (1)$$

where m_i is the mass of the pedestrian and τ is a typical relaxation time parameter that characterizes the time spent by a pedestrian to reach the direction \mathbf{e}_i and speed v_i^0 . In general, v_i^0 depends on the position \mathbf{r}_i of the pedestrian, i.e., geometry-dependent, or can even be different for each individual by definition¹¹.

\mathbf{f}_{ij}^s is the inter-pedestrian pairwise social force, which is of repulsive nature and stems from the idea that a pedestrian i is prone to avoid colliding with another pedestrian or an obstacle j . Therefore, a widely-used and simple alternative to mimic this behavior relies on selecting a decaying function for \mathbf{f}_{ij}^s as a function of the distance between the pedestrian i and another pedestrian or obstacle j , $\mathbf{r}_{ij} = \mathbf{r}_i - \mathbf{r}_j$. Although there are more

¹Basque Center for Applied Mathematics (BCAM), Alameda Mazarredo 14, 48009 Bilbao, Spain. ²Department of Mathematics, University of the Basque Country UPV/EHU, P.O. Box 644, 48080 Bilbao, Spain. ³KERBASQUE, Basque Foundation for Science, Calle María Díaz de Haro 3, 48013 Bilbao, Spain. ⁴Zienkiewicz Center for Computational Engineering (ZCCE), Swansea University, Bay Campus, Swansea SA1 8EN, UK. ✉ e-mail: dhernandez@bcamath.org; mellero@bcamath.org

complex anisotropic functions to model anticipation and limited visual range effects^{5,12–14}, we use the standard circular specification here, consisting of an isotropic decaying exponential function with two parameters A and B . Hence, the social force between two agents is described by

$$\mathbf{f}_{ij}^s = Ae^{-\frac{|R_{ij}-r_{ij}|}{B}} \frac{\mathbf{r}_{ij}}{|\mathbf{r}_{ij}|}, \quad (2)$$

with A and B accounting for the strength and range of the force, respectively. In the present work, pedestrians are modeled as disks, and $R_{ij} = R_i + R_j$, being R_i and R_j the radii of agents i and j .

Finally, \mathbf{f}_{ij}^c mimics those forces that appear when two agents are in physical contact, that is to say, when $|\mathbf{r}_{ij}| < R_{ij}$. Pedestrian systems usually experience contact forces in high-density scenarios where social forces cannot keep pedestrians apart. For this reason, the contact force becomes especially relevant in crowded systems or when pedestrians are in a rush. Under the last circumstances, the values of the desired force term can increase dramatically, overcoming social forces. Helbing and Molnár proposed \mathbf{f}_{ij}^c as the sum of two contributions $\mathbf{f}_{ij}^c = \mathbf{f}_{ij}^B + \mathbf{f}_{ij}^S$, a compressing spring-like force

$$\mathbf{f}_{ij}^B = H\delta_{ij} \frac{\mathbf{r}_{ij}}{|\mathbf{r}_{ij}|}, \quad (3)$$

and a shear force that introduces friction due to the contact force

$$\mathbf{f}_{ij}^S = -\gamma\delta_{ij}(\mathbf{v}_{ij} \cdot \mathbf{t}_{ij})\mathbf{t}_{ij}, \quad (4)$$

where $\delta_{ij} = R_{ij} - |\mathbf{r}_{ij}|$ is the overlap between the interacting agents. H and γ are the compression and shear parameters, respectively. \mathbf{v}_{ij} is the relative velocity between pedestrians i and j , and \mathbf{t}_{ij} is the vector tangential to \mathbf{r}_{ij} . It is worth mentioning that the overlap must fulfill $\delta_{ij} \geq 0$; otherwise, both contact contributions are null.

Previous attempts to elucidate the mechanism underlying FIS have primarily relied on the microscopic structure of the particles forming part of the pedestrian system^{15,16}. The predominant argument appeals to the fact that when particles are flowing, *blocking structures* are prone to arise. These blocking clusters are associated with an increase in the clogging probability, indicating that forming these clusters is necessary for the emergence of FIS. Due to the resemblances of these concepts with the extensively studied arch formation and clogging in granular matter physics, most of the precedent research on disentangling FIS stems from established frameworks of the above-mentioned field. Nevertheless, since most granular experimental systems consider inert particles, no physical cause prevents the formation of the above structures¹⁷, and additional factors should be contemplated. Such is the case studied in refs. 8,18, where a quasi-2D granular system was assessed so that the driven force is a control parameter obtained by varying the incline angle between the plane where particles are contained and the horizontal one. Additionally, the authors incorporated a horizontal oscillation that can prevent or break the arches, obtaining evidence of FIS for inert particles. This outcome implies that a physical mechanism able to prevent or break arches is necessary. Pastor et al.⁸ explained the FIS as a combination of flowing and clogging states. Other studies have considered a distinct way of breaking or avoiding arches by introducing a noise for the rotation dynamics of non-circular pedestrians^{10,19}.

Recently, Cornes et al. showed that evacuation and, as a consequence, frictional clogging times correlate well with the size of the clusters, claiming that the appearance of FIS owes to the presence of medium-size clusters that coincide with the typical size of the blocking clusters²⁰. In that contribution, a blocking cluster is defined as a pedestrian group in which each individual possesses contact with another of the same group, and two particles from the cluster are in contact with the walls at both sides of the exit. Then, for higher-driven forces, the probability of emerging medium-size clusters reduces, making it more likely to find a combination of small and large clusters. Also, small clusters are present for all desired velocities, even though it is

demonstrated that their number is much lower after the optimal evacuation time. When inert particle flow through a silo is analyzed, it is usual to observe dense scenarios. Thus, small or medium clusters are rarely obtained in pedestrian evacuation. As stated recently²⁰, the pedestrian system is expected to behave as a single geometry-spanning cluster for larger driven forces being similar to a highly viscous fluid.

There is a paucity of evidence on the rheology of pedestrian crowds in the literature, although if one carefully analyzes pedestrian and (non) Brownian suspensions, strong analogies arise. The desired force is identical to a viscous (Stokesian), similar to those considered for (non)Brownian suspensions^{21–23}. In suspension systems, repulsive electrostatic forces, usually described through DLVO theory, resemble pedestrian social forces, whereas contact forces materialize when particles are forced into touch, similarly to \mathbf{f}^c considered in the SFM. However, in the model introduced by Seto et al., lubrication forces are included for the numerical simulation of suspensions, an ingredient that is not considered in the present version of the SFM or either in a previous work where shear thickening was evidenced for frictional particles under a Stokesian drag force²³. (Non)Brownian suspensions can be described as non-Newtonian fluids, i.e., their viscous response under external forces is nonlinear, presenting a complex behavior. Special relevance covers those systems that flow worse as the outside perturbation increases, with this rheological effect being known as *shear thickening* (ST)^{24–28}. This observation shows an augment in the effective viscosity η_{eff} of suspensions. The η_{eff} increase can be either continuous or abrupt, i.e., related to continuous shear thickening (CST) and discontinuous shear thickening (DST), respectively. The transition from CST to DST strongly depends on the concentration of particles in the suspension^{21,22,29–32} and the friction characteristic of the particles^{33,34}.

Based on the elements previously proposed by Seto et al.²¹ examining shear thickening for particulate suspension flows, Wyart and Cates (WC) introduced a phenomenological theory that considers a crossover from frictionless (lubricated) interactions to frictional contacts³⁰. This crossover is characterized by an *onset stress* σ^* , at which weak repulsive forces (e.g., DLVO) fail to prevent particles from touching, and a lubrication-to-frictional transition occurs. Following this reasoning, if the total stress in terms of the onset stress is low ($p = \sigma/\sigma^* \ll 1$), the system's viscosity diverges at the random close packing fraction ϕ_0 typical for frictionless systems. Conversely, if $p \gg 1$, most of the contacts become frictional, and η_{eff} diverges at a packing fraction $\phi_m < \phi_0$, whose precise value depends on the characteristic static friction coefficient of the contact pairwise interactions. In the WC model, the rheology of dense (non)Brownian suspensions is described through a jamming volume fraction $\phi_j(p)$, which is taken to depend on the fraction of frictional contacts through a function $f(p)$ that evolves smoothly from 0 to 1 within the domain $p = [0, \infty)$. In this way, jamming volume fraction $\phi_j(p)$ takes the form

$$\phi_j(p) = \phi_m f(p) + \phi_0(1 - f(p)). \quad (5)$$

Other more recent frameworks have been introduced to describe DST, considering an inverse-biviscous model³⁵, scalar WC model³⁶, or developing the WC model with the inclusion of a full tensorial evolution equation³⁷. With regard to $f(p)$, multiple mathematical functions have been considered in the literature^{30,38,39}. Nevertheless, the most widely accepted and experimentally proven³¹ is

$$f(p) = \exp\{-(1/p)^\beta\}, \quad (6)$$

where the exponent β describes how steeper the frictionless-to-frictional transition is. At dense scenarios, DST models consider that the viscosity η diverges following a Krieger–Dougherty expression⁴⁰ as a function of $\phi_j(p)$ and the volume fraction ϕ

$$\eta(\phi, p) \sim (1 - \phi/\phi_j(p))^{-\lambda}, \quad (7)$$

where λ is typically estimated with the value 2.

In the present contribution, we aim to elucidate the nature behind FIS on the basis of the forces involved in the dynamics. On the one hand, the social forces mimic the long-range interaction of pedestrians to sidestep each other and avoid touching. On the other hand, contact frictional forces might occur if the weakly repulsive social forces fail to maintain pedestrian inter-distance larger than their physical sizes. It is precisely this transition from pedestrians interacting only socially to pedestrians contacting frictionally that induces the FIS phenomenon. A systematic understanding of how the distinct forces contribute to the emergence of FIS is still lacking. To fill this gap, an adequate approach, hitherto unexplored, consists of employing tools and understanding from the field of suspension rheology. This can be a significant change in perspective since it implies that experiments using specifically tuned suspensions can be used to mimic pedestrian behavior. Moreover, utilizing theory and numerical models rooted in suspension investigations can shed new light and revisit the field of pedestrian dynamics from a new rheological perspective. In this work, we demonstrate that it is possible to translate shear thickening into push faster is the slower picture in pedestrian systems governed by a social force model, establishing a direct link between ST and FIS concepts.

Results

Flow rate

Firstly, we analyze the number of pedestrians that exit the room during the total time of the simulation. As the first result, we obtain that the system flows for each desired velocity considered here when the width of the exit $b \geq 2D_m$, where D_m is the mean diameter of the $N = 300$ polydispersed pedestrians. On the contrary, for smaller apertures, the pedestrians are prone to clogging in the vicinity of the exit, and as a consequence, the flux is stopped (see, as an example, the snapshot displayed in Supplementary Figs. 1 and 2) in Supplementary Note 1. In previous investigations, rotational noise was applied on pedestrians to prevent permanent clog formation^{10,19}. One way of rationalizing the effect of the desired velocity v^0 on evacuation time is to find the inverse slope of the cumulative number of egressed pedestrians N as time t goes by (see Supplementary Fig. 2b) and see how the time it takes for a pedestrian to leave Φ varies. Therefore, in order to find the best linear fits of the time magnitude as a function of the number of pedestrians who escape through the bottleneck, we constructed the plot of Fig. 1a. Note that the procedure to obtain the characteristic *evacuation time* Φ is done by finding the slope of the time t as a function of the egressing pedestrians number N (t vs. N) and not N vs. t . The non-monotonicity of Φ is evident for each exit size, confirming the existence of FIS since the evacuation is faster when the desired velocity is increased from the minimum v^0 m/s to a critical desired velocity v_c^0 ($v_c^0 = 1.125$ m/s for $b = 2D_m$ and

$v_c^0 = 1.25$ m/s for $b = 3D_m$). The evacuation becomes slower after this value up to $v^0 = 5.0$ m/s. Finally, for larger values, the evacuation becomes faster again. The mentioned trend is reproduced for all the b values, while it is true that it is more pronounced for the case $b = 2.0D_m$.

Analysis of the macroscopic flow near the exit

As was shown in Fig. 1a, the exit size $b = 2D_m$ is the case that exhibits the most amplified FIS phenomenon. Nonetheless, this exit width can exhibit instabilities and extreme clogging when other force configurations are studied. Hence, in order to avoid biases in the statistics, we consider the bottleneck $b = 3D_m$ and apply post-processing with the coarse-graining technique. Selecting this exit width bottleneck allows us to describe the system akin to shear-jammed particulate systems²¹. In this sense, we computed the average of the coarse-graining spatial profiles in a centered rectangle of dimensions $2D_m \times 2D_m$ located in front of the exit, \mathcal{A} .

The flow rate is a magnitude that depends on two quantities: the pedestrian filling fraction $\phi(t)$ and the perpendicular velocity of the pedestrian near the gateway $v_x(t)$ through the relation $1/\Phi \sim \phi v_x$. From the independent examination of these magnitudes, it is possible to elucidate if the overall evacuation time is affected by a variation of one of the two magnitudes or if the variation is due to a combined effect. Let us focus only on the values of $\bar{\phi}$ in Fig. 1b (orange-colored squares, right y-axis). This plot shows that the time- and spatial-averaged area fraction surrounding the exit $\bar{\phi}$ follows a monotonic increase with the desired velocity. In that case, the conclusions we might extract contradict the results of Fig. 1a since the inverted flow rate trend differs from the monotonic one, even when they are directly proportional. Thus, the behavior of time-averaged velocity \bar{v}_x should be such that it reverts the $\bar{\phi}$ trend observed for Φ . That is, \bar{v}_x values must be lower in the cases of higher density and more significant for the most dilute cases in order to recover the FIS flow rate trend, observed in Fig. 1a.

The growth of $\bar{\phi}$ presents two different slopes: for low desired velocities, $v^0 < 1.25$ m/s, the area fraction holds a higher growth compared to the trend observed for $v^0 \geq 1.25$ m/s. This outcome could be connected to a transition in the pedestrian dynamics related to a variation in the balance of social and contact forces. Although one might expect for a realistic situation that the area fraction reaches a constant value at some point in the studied v^0 range, the density is constantly increasing. This result could be due to the selection of model parameters or the simplicity of the contact model, which allows excessive overlaps between pedestrians. Fig. 1b exhibits the time-averaged velocity in the x -direction \bar{v}_x (blue-colored circles, left y-axis), evidencing a trend that is consistent with the result observed for the flow rate with a maximum for \bar{v}_x at $v^0 = 1.25$ m/s, which corresponds to the fastest

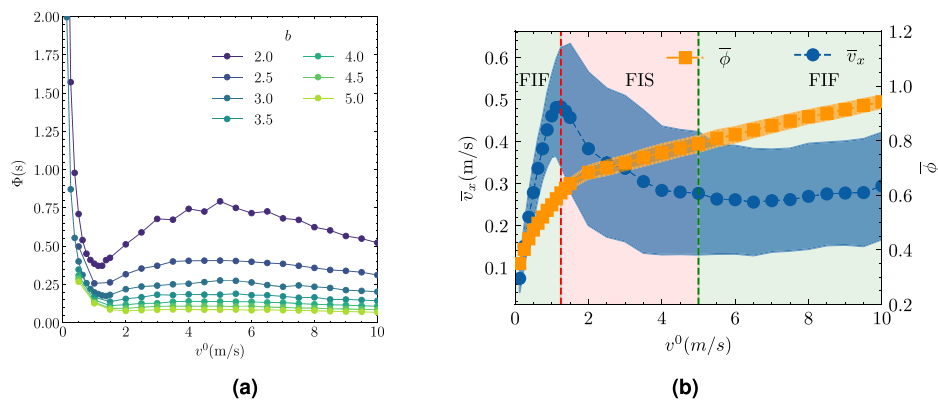


Fig. 1 | Mean flow rate for a pedestrian and depending variables velocity and density. a Averaged time that it takes for a pedestrian to exit the room or single pedestrian evacuation time Φ as a function of the desired velocity v^0 for each aperture b in terms of D_m units. Each point is the best linear fit slope of t vs. N , with standard errors more minor than the marker size for all values. **b** Time-averaged area fraction $\bar{\phi}$ (orange-colored squares, right y-axis) and velocity \bar{v}_x (blue-colored circles, left y-

axis) as a function of the input desired velocity v^0 for $b = 3.00D_m$. The colored areas stand for the standard deviation for $\bar{\phi}$ and \bar{v}_x . Shadowed red and green areas distinguish the faster-is-faster (FIF) from faster-is-slower (FIS) behavior. The cross-overs between distinct behaviors are highlighted with the vertical dashed lines placed at $v_c^0 = 1.25$ m/s (red) and $v_c^0 = 5.0$ m/s (green).

evacuation. Furthermore, the minimum value around $v^0 = 5.0$ m/s also reproduces the flow rate behavior. From this outcome, the conclusion is that the change in evacuation times for $v^0 \leq 5.0$ m/s, as well as the onset of FIS, are due to changes in the near-exit velocity of the flow rather than area fraction, even though these magnitudes can be related. On the other hand, for $v^0 > 5.0$ m/s \bar{v}_x is almost invariable independently of the increase of the desired velocity, and the emergence of the second FIF, with a slight increase of the flow rate area, is due to the increase in density as a function of v^0 . The value where the $\bar{\phi}$ and \bar{v}_x trends vary their behavior, specifically, the changes in the slope for $\bar{\phi}$ and the monotonicity for \bar{v}_x matches.

These results indicate that the FIS is due to a non-monotonic variation of the flow velocity close to the orifice as a function of the desired velocity, which is connected to a change in the slope of the monotonic trend for Φ . The next question, therefore, arises: what are the rheological changes of the crowd that are affected by the competitiveness and lead to the mentioned FIS behavior? Firstly, we analyzed their values separately to shed light on the effect of the distinct force contributions. Figure 2a displays the social and contact pressure from Eq. (11) time- and spatially averaged as in the previous analysis (P_s and P_c , respectively). Both trends, P_s and P_c show a linear growth with the increase of v^0 for $v^0 > 1.5$ m/s. With this result, it is confirmed that the transition in the dynamics stems from the activation of contact forces between pedestrians that become increasingly significant. In fact, the values of P_c are close to zero for low competitiveness due to the area fraction being low; for larger v^0 , the contact forces appear as a result of the density increase. This can also explain why the evacuation becomes slower for v^0 values higher than 1.25 m/s. Unlike P_c , P_s differs from zero at every v^0 and increases monotonically from the simulated minimum v^0 . Comparing both trends manifests a crossover just after the value of v^0 , where the evacuation is the slowest ($v^0 = 5.0$ m/s). This result suggests that the evacuation starts to be faster again because the contact pressure overcomes the social pressure. Also, this result is in correspondence with the recent findings shown²⁰, where the authors connected the transition to faster-is-faster to the formation of a big cluster encompassing almost all the pedestrians and forcing the system to flow as a whole with a diminishing of the clogging. The decrease in the clog times must also occur due to a reduction of the system friction. We analyze the near-exit friction of the system later in this contribution.

Centering the attention on the P_s trend, it is also possible to observe that this is very similar to the profile of $\bar{\phi}$ as a function of v^0 . Finally, figure 2a depicts the total pressure, showing a linear increase as a function of the desired velocity. From this outcome, we can conclude that the increase in the desired velocity always provokes a linear increase in the total pressure despite the change in the slope of the different force contributions.

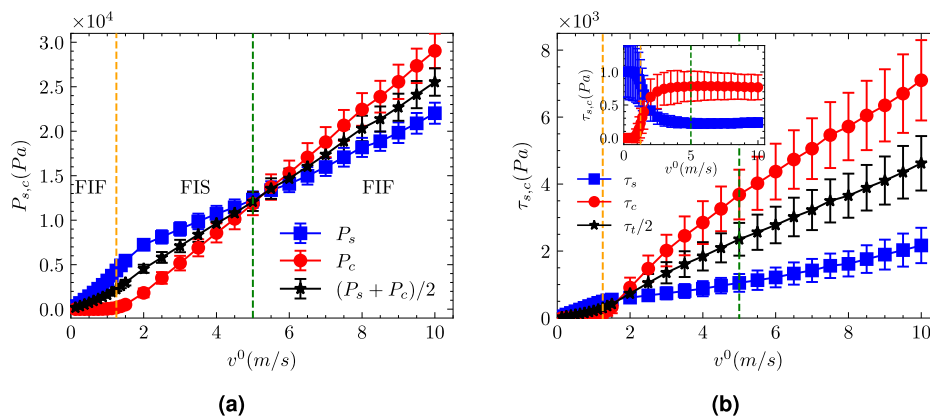


Fig. 2 | Pressure and shear stress close to the exit. For the exit width $b = 3.00D_m$: **a** Plot of time-averaged contact and social pressure P_c (red circles) and P_s (blue squares), respectively, as a function of the desired velocity v^0 . As a reference, the total pressure contribution divided by two is plotted (black stars), showing a monotonic linear increase with v^0 . **b** Plot of time-averaged the deviatoric part of the contact and social stress τ_c (red circles) and τ_s (blue squares), respectively, as a function of the

Complementary, we have mapped the total pressure with the local area fraction, showing that the pressure collapses in a single curve that increases monotonically with the increment of the area fraction (see Supplementary Fig. 4a), as expected. Conversely, the total pressure near the exit does not show that collapse since the system releases the pressure depending on the preceding pressure in addition to the area fraction.

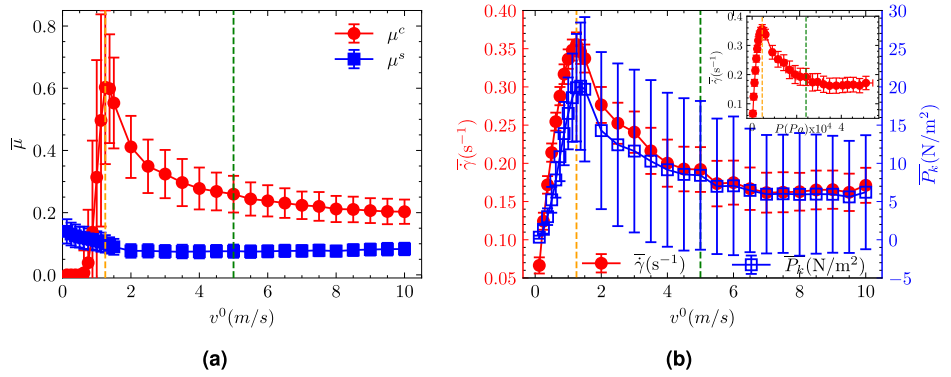
For the sake of completeness, we extracted the deviatoric part of the stress tensor τ_t and also split it into the social and contact contributions, τ_s and τ_c . This component of the stress is critical to the understanding of either the evacuation slowdown or thickening suspension since these are forces transmitted laterally to the flow direction. Thus, high values of τ_t may imply a proliferation of frictional contacts and a frictionless-to-frictional interaction transition. The result of averaging these quantities close to the exit is illustrated in Fig. 2b. The inset in Fig. 2b additionally displays the fraction of shear stress from the social interaction, τ_s/τ_t , or from the contact, τ_c/τ_t . Both trends show a clear symmetry and tend to reach a constant behavior for $v^0 > 5$ m/s. The crossover of the deviatoric part of the contact tensor on the social one occurs again close to $v^0 = 1.85$ m/s. From this observation, we can infer that FIS arises when the frictional contribution of the contact forces becomes relevant. Nonetheless, a full picture of the effect of the contributions of the pressure and the deviatoric parts must be described by the friction coefficient. This analysis is presented in the following section.

Rheology of the system

The rheology of a pedestrian system can be characterized either through the overall viscosity Eq. (14) or via a macroscopic friction coefficient Eq. (15). μ Rheology—by focusing first on the latter, we show in Fig. 3a the time- and spatial-averaged profile of the contact $\bar{\mu}^c$ and social $\bar{\mu}^s$ friction coefficient (Eq. (15)) as a function of the desired velocity. As expected, $\bar{\mu}^c$ is zero for low velocities due to the contact force being zero. In this sense, the values that are different from zero always present contacts near the exit. One can notice that the values decrease after the maximum value is reached, which, again, is close to the v^0 value at the fastest evacuation. Astonishingly, the $\bar{\mu}^c$ trend is counterintuitive to explain the FIF and FIS zones if we rely solely on it since one may expect that the macroscopic friction should increase as the evacuation becomes slower. Nevertheless, connections between the decrease in the macroscopic friction and the occurrence of jamming with the contact network anisotropy have been verified in the past when studying the shear jamming of granular materials^{41,42}. Our results here confirm that the $\bar{\mu}^c$ diminishes as the contact network becomes more isotropic, as shown in Supplementary Note 3. The decrease of macroscopic contact friction has also been recently proven to be linked with the increase of suspension viscosity in DST by Thomas et al.⁴³. An additional cause can be attributed to

desired velocity v^0 . The total deviatoric part of the stress is shown as a reference (black stars). Inset: the fraction of shear stress from the social interaction, τ_s/τ_t (blue squares), or from the contact, τ_c/τ_t (red circles). In both a and b, including the inset, orange and green lines have been included to distinguish the faster-is-faster (FIF) from faster-is-slower (FIS) behavior. Error bars depict the standard deviation values.

Fig. 3 | Friction and shear rate behavior near the exit. **a** Spatial- and time-averaged contact (red circles) and social friction (blue squares) parameters ($\bar{\mu}^c$ and $\bar{\mu}^s$) as a function of the desired velocity v^0 . **b** Spatial and time-averaged $\bar{\gamma}$ (red-colored circles, left y-axis) and kinetic pressure \bar{P}_k (blue-colored squares, right y-axis) as a function of the desired velocity v^0 . The inset displays $\bar{\gamma}$ against the total pressure P averaged in the area of interest. In both **a** and **b**, including the inset, the considered case is $b = 3D_m$, and orange and green lines have been included to distinguish the faster-is-faster (FIF) from faster-is-slower (FIS) behavior. Standard deviation values are illustrated via error bars.



the behavior of the kinetic pressure \bar{P}^k (see Fig. 3b), which measures the velocity dispersion. More in detail, along the FIS zone, the ratio between the dissipative term in the interactions (Eq. (4)) diminishes compared to the gain of the elastic part Eq. (3), given that the velocity dispersion decreases.

In terms of social friction coefficient, $\bar{\mu}^s$ shows to be higher at low desired velocities and then tends to decrease, reaching a constant value $\bar{\mu}^s \approx 0.08$. The origin of $\bar{\mu}^s$ is rooted in two distinct mechanisms related to an imbalance of social forces acting on a single pedestrian. On the one hand, pedestrians close to the exit experience a shear due to wall forces, which do not have a force pair, provoking an imbalance. On the other hand, a particle that is near the egress can affect the balance of forces due to instabilities in the equilibrium between the desired force and the social force in this zone. This effect can provoke clogging delays due to social interactions²⁰, and it is especially important in dilute scenarios when the competitiveness is still low. A crucial conclusion we can extract from this outcome is that FIS seems to be directly connected to an increase in the frictional shear forces relative to the normal forces. As the friction shear forces increase compared to the normal forces, FIS must be enhanced because these forces push the particles away laterally from the desired direction. Thus, the tangential term of the contact force plays a crucial role.

The contact tangential term depends on the relative velocity of pedestrians in contact. Therefore, one should anticipate that the increase in this term has to be related to the presence of fluctuations in the velocities as well as a higher shear rate. This expectation is confirmed through the curves of the kinetic pressure and the shear rate in Fig. 3b. The outcome reveals similar behavior for both magnitudes, having maximum values close to the desired velocity value where FIS is raised. This outcome also reveals that the shear rate can return an identical value for two distinct v^0 or, keeping in mind that the total pressure P scales linearly with v^0 , two different P present in the system. This reasoning is confirmed with the inset of Fig. 3b which displays the shear rate $\dot{\gamma}$ as a function of P with identical behavior to the $\dot{\gamma}(v^0)$ trend. From the rheological point of view, the observation of a multivalued $\dot{\gamma}(P)$ profile becomes relevant since it means that not only the system's response is non-Newtonian but also evidence of a complex response of a discontinuous shear thickening type^{30,44}. This can be better understood by noting that there is a maximum value of $\dot{\gamma}$, i.e., $d\dot{\gamma}/dP = 0$. Thus, there is a domain of v^0 , where $d\dot{\gamma}/dP > 0$, indicating that the system flows easier with the pressure increase, whereas, at a certain point, $d\dot{\gamma}/dP$ becomes negative, implying an increase of the viscosity and, as a consequence, an arresting of the flow. This change results from the triggering of contact forces, making the system thicker.

One aspect we still need to address up to this point is that the current experimental setup is typical for studying clogging⁴⁵. Clogging is a flow halt, typically observed when a particulate matter crosses a constriction⁴⁶. However, DST has been primarily connected to jamming transition, which characterizes a liquid-like to solid-like transition for granular materials^{41,47}. Nowadays, there is consensus on the distinction between both phenomena, albeit they present a common underpinning mechanism of force chain formation. Unlike clogging, which presents local characteristics with the

formation of local structures that arrest the succeeding flow, jamming comprises a global state that exhibits ordering in the force network space⁴⁸. This observation has also been established as a microscopic origin for shear thickening in dense granular suspensions⁴³, and it is related to the concept of rigidity percolation that has been linked to DST very recently⁴⁹. Apart from jamming by compression, granular systems can exhibit shear jamming and an intermediate state called fragile differentiating in the ability of whether the system can bear incompatible loads⁵⁰⁻⁵². Bi et al. showed that shear jamming and fragile states are distinguished by a transition in the force percolation length in shear and compression direction⁵¹. While the former is characterized by an entire force percolation throughout the system, the percolation only occurs along the compression direction in the latter. It is worth mentioning that DST has also been recently evidenced for dry granular systems under oscillatory shear experiencing not only shear jamming but also a fragile state⁵³, and Seto et al. showed that the shear jamming states in suspensions can truly evolve in fragile systems when reversed shear is applied⁵⁴.

Despite the discussed distinction between clogging and jamming, determining whether one phenomenon or another is dominant is still an open question in systems where both can arise simultaneously, such as the particle flow through a bottleneck. Recent contributions have been devoted to finding connections between both phenomena⁵⁵⁻⁵⁷, advancing their understanding, even though a valid theoretical framework or method to distinguish them is still lacking. Following the analysis performed by Bi et al.⁵¹, we conducted a force percolation analysis for the strong force network, defined as the contact forces bearing more than the average contact force magnitude for the whole system ($|f^c| > \langle |f^c| \rangle$) (see Supplementary Note 3 and Supplementary Fig. 9). Since the particles grouped around the exit resembles a semicircle, we split the percolation directions into radial and azimuthal directions. From this analysis, we argue that the radial percolation length reaches zones at a considerable distance from the exit, which increases with the desired velocity. Although the radial percolation does not extend to the whole system, this result indicates that the force chains do not appear just locally, as would be the case of pure clogging. Complementary to this is that the azimuthal direction increases with the desired velocity, as does the radial direction. This last result should also be observed in the case of clogging when stable arches are formed. Nonetheless, these percolation lengths were extracted during the time for several configurations and remained statistically greater than zero. Together with the decline of the contact network anisotropy and the growth of frictional contacts as a function of the desired velocity, these results suggest that the system's behavior depends on bulk properties rather than a local phenomenon such as clogging merely. We consider that further investigation is required in order to characterize whether the system is experiencing a shear jamming or fragile state. An excellent approach to carry out this task is the theoretical framework proposed by Ramola and Chakraborty to include body forces acting on the particle system and evaluate the persistence of the contact force network⁵⁸. We remark that this framework has been employed in granular suspension, allowing the understanding of the microscopic origin of DST⁴³.

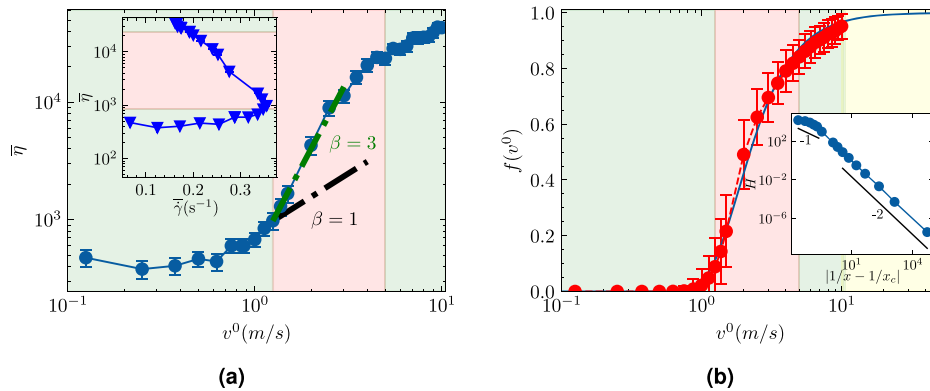


Fig. 4 | Viscosity and frictional contact fraction increase as a function of the desired velocity. **a** Spatial and time-averaged viscosity η as a function of the desired velocity v^0 . The slopes $\beta = 1$ and $\beta = 3$ have been included as guides for the eye. β characterizes the exponent in the relationship $\eta \sim P^\beta$, here $P \sim v^0$. Thus, $\beta = 1$ implies an invariable shear rate with the increase of P ; and $\beta > 1$ implies a multivalued dependency $\eta(\dot{\gamma})$ as is obtained in this case, assuming $\dot{\gamma} \sim P/\eta$. The inset depicts the multivalued dependency $\eta(\dot{\gamma})$. **(b)** Spatial and time-averaged fraction of frictional contacts as a function of the desired velocity v^0 , $f(v^0) = \exp\{-(v_c^0/v^0)^\beta\}$ is plotted, showing a good agreement with the numerical data. The

critical desired velocity $v_c^0 = 1.85$ m/s and the exponent $\beta = 2$. The inset displays the function $\mathcal{H} = \eta f(p)^2$ versus $|1/x_c - 1/x|$; the black lines stand for exponents -1 and -2 as annotated. All cases correspond to $b = 3D_m$, and shadowed red and green areas have been included to distinguish the faster-is-faster (FIF) from faster-is-slower (FIS) behavior. In the specific case of **b**, an additional yellow-colored range is plotted exclusively to depict the shape of $f(v^0)$ at larger v^0 values. Error bars stand for the 95% confidence interval and are not shown when they are less minor than the marker size.

Furthermore, we consider that the current discussion can motivate the investigation of connections between DST and suspension systems prone to clogging⁵⁹.

η Rheology—When considering a three-dimensional scenario, passive spherical particles suspended in a solvent with viscosity η_0 display an effective dimensionless viscosity, $\eta_{\text{eff}} = \eta/\eta_0$, that is dependent on the volume fraction. Krieger and Dougherty’s semi-empirical law provides a reliable description of this relationship⁴⁰. In a two-dimensional system, similar behavior should occur, obtaining. As a result, an increase of η_{eff} as the area fraction is augmented. Thus, as the increase of the desired velocity is linked to a monotonic increase of ϕ , this might imply by itself a gain in the effective viscosity. Fig. 4a shows the viscosity as a function of the desired velocity. For low desired speeds $v^0 < 1$ m/s, the social force can maintain the particles apart without physical contact (social contactless regime); therefore, they can move easily in the absence of shear forces. Consequently, the viscosity η remains almost constant despite the small increase in area fraction. However, when $v^0 > 1$ m/s, it is unviable for the social force to keep the particles distant, frictional contacts set in (frictional contact regime), and the viscosity increases significantly. This scenario is in agreement with recent theories of shear thickening in wet particle suspensions as a result of a frictionless-to-frictional transition mediated by a variable weak repulsion force^{21,29,30}. The role played by a weak repulsive force determining the energy barrier for contactless against contact interactions is here taken by the screening social force model.

Figure 4a also shows that the steep increment of η as a function of v^0 follows the relation $\eta \sim (v^0)^\beta$, with $\beta = 3$ indicating a multivaluated dependency $\eta(\dot{\gamma})$. A relationship with $\beta > 1$ indicates a multivaluated dependency $\eta(\dot{\gamma})$ ^{32,60} since it means the shear starts to decrease with the increase of the stress (as it was shown in Fig. 3b), and it is considered to be a hallmark of DST. The inset of Fig. 4a stresses this argument since $\eta(\dot{\gamma})$ shows a multivalued behavior. Both observations, the fact that $\beta > 1$ and the multivalued behavior of $\eta(\dot{\gamma})$, constitute evident fingerprints of DST. In Supplementary Note 2, a complementary analysis of the local viscosity as a function of the local pressure has been performed, showing that the DST transition not only emerges in the area surrounding the exit but also in the bulk system (see Supplementary Fig. 4b). This observation is also suggesting that a transition far from exit and beyond clogging arises in the system, such as an unjammed to a shear-jamming or fragile state.

To verify the compatibility of the WC model with the results, we have computed the fraction of frictional contacts for each simulated desired velocity $f(v^0)$. Here, $f(v^0)$ is evaluated using the same definition lately

proposed by Ruiz-Lopez et al.⁶¹, that is, the fraction of particles having at least one contact in friction. In this case, the particles that meet the criteria overlap and have a relative tangential velocity different from zero. The particles analyzed are contained in the area \mathcal{A} . Figure 4b displays the time-averaged $f(v^0)$, showing to be in agreement with the function $f(v^0) = \exp\{-(v_c^0/v^0)^\beta\}$, defining v_c^0 as the critical desired velocity. From the inset of Fig. 2b, we have identified $v_c^0 = 1.85$ m/s as the value where the contact shear stress overcomes the social shear stress. Moreover, the exponent $\beta = 2$ recovers the behavior of the numerical results of $f(v^0)$. This agreement between the numerical results and the analytical function gives insights into the possibility of modeling pedestrian systems using the WC model. Nonetheless, the fraction of frictional contacts depends on both the total pressure imposed over the system and the local area fraction, variables that are dependent on the desired velocity (see Supplementary Note 2). This reasoning implies the possibility of a combined effect for the viscosity increase led by either density or pressure augments. Thus, we conduct a scaling analysis to avoid this ambiguity.

A recent study⁶² proposed a universal scaling for shear thickening transitions. In this work and other⁶³, the authors employed the scaling in equilibrium phase transition framework⁶⁴ rather than fitting data to functional forms. The scaling framework allows for collapsing data over a broad range of multiple control parameters, resulting in a tool extremely useful in systems such as the current one where both density and stress vary with the parameter of control v^0 . They described shear thickening in terms of a crossover between the two critical maximum solid volume fractions ϕ_0 and ϕ_m , points where the viscosity following Eq. (7) diverges. They proceeded by substituting Eq. (5) into Eq. (7), yielding

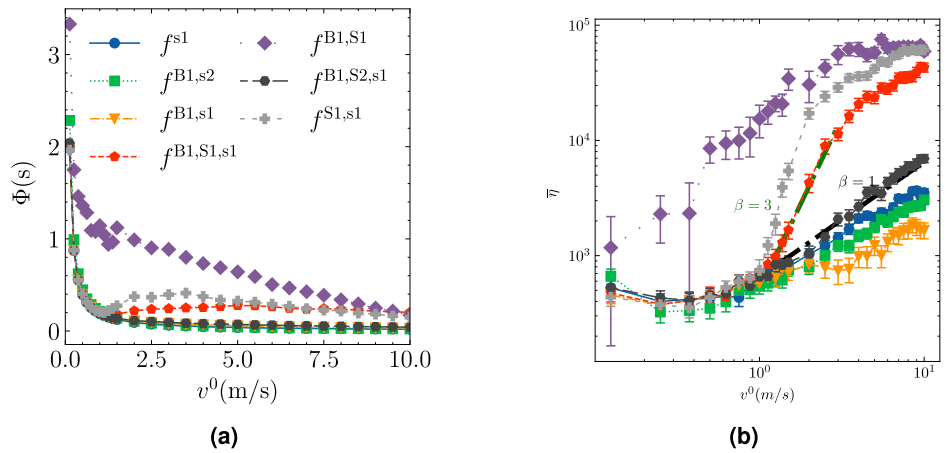
$$\eta(\phi_0 - \phi)^2 \sim \mathcal{F}_{\text{WC}}\left(\frac{f(p)}{\phi_0 - \phi}\right), \mathcal{F}_{\text{WC}} \sim \left(\frac{1}{\phi_0 - \phi_m} - \frac{f(p)}{\phi_0 - \phi}\right)^{-2}, \quad (8)$$

where \mathcal{F}_{WC} is the crossover scaling function specific to the WC model with the scaling variable $x_{\text{WC}} = f(p)/(\phi_0 - \phi)$ related to the frictionless jamming critical point, and $x_c = 1/(\phi_0 - \phi_m)$ is the critical point at which \mathcal{F}_{WC} diverges. Following the work of Cardy⁶⁴, Ramaswamy et al.⁶² write the scaling in terms of a universal function \mathcal{H} as follows:

$$\eta g^2(p, \phi) \sim \mathcal{H}(|1/x_c - 1/x|), \quad (9)$$

where the function g is more general than the function $f(p)$, expanding the transition dependence to density besides the stress^{62,63}. The scaling analysis

Fig. 5 | Correspondence between FIS and shear thickening in terms of the flow rate and the viscosity. **a** Averaged time that it takes for a pedestrian to exit the room as a function of the desired velocity for the force settings described in the section “Numerical setup: room scape scenario”. Each point is the best linear fit slope of t vs. N . **b** Spatial and time-averaged viscosity η as a function of the desired velocity v^0 , colors and symbols match the ones represented in (a). The slopes $\beta = 1$ and $\beta = 3$ have been included as guides for the eye. Error bars stand for the 95% confidence interval and are not shown when they are less minor than the marker size.



of \mathcal{H} is relevant since changes in its exponent underpin differences in the frictional shear-jamming and frictionless jamming transition, indicating a crossover between critical values that belong to different universality classes. As the function g can depend on p and ϕ , we can use the universal scaling to parse out the pressure and density. Firstly, in Supplementary Note 4, we have estimated the value of $\phi_0 = 0.959 \pm 0.001$ and demonstrated that \mathcal{F}_{WC} diverges at a point $x_c = 1/(\phi_0 - \phi_m) = 4.927$, from which it is obtained $\phi_m = 0.756 \pm 0.001$. The inset of Fig. 4b depicts the behavior of the universal scaling function $\mathcal{H} = \eta f(p)^2$ versus $|1/x_c - 1/x|$, denoting a clear change in the exponent. This outcome demonstrates that crowds are governed by two distinct critical points similar to the DST transition with two distinct jamming criticalities (one frictionless and the other frictional).

Disentangling the influence of force nature in FIS

The following final analysis is dedicated to shedding light on the type of interactions involved in the model that induces FIS. With this aim, we consider the sets described in the section “Numerical setup: room scape scenario”. Figure 5a shows the average time a pedestrian takes to exit the room as a function of the desired velocity for aperture $b = 3D_m$. Within these sets, only two of them yield FIS, namely $f^{s1,s1}$ and $f^{B1,S1,s1}$. These two cases have the presence of the shear force term given by Eq. (4) in common, and it is noticeable that the case with the f^b deactivated enhances the FIS phenomenon. A similar result to the last one was previously found⁶⁵.

Neither the sets where the particles solely interact due to social forces nor contact forces alone can influence the emergence of FIS. However, the latter case behaves distinctly to the rest of the cases. Under these circumstances, the absence of social force induces particles to enter into contact starting from low velocities in contrast to the cases when social forces are contemplated. It is worth mentioning that all these results clearly show that FIS is obtained only if social and shear forces are included in the model, with the social forces being responsible for the transition from contactless to contact frictional. The outcome reveals that substantial values of shear force are needed to observe FIS, i.e., contact forces solely do not trigger FIS.

Paying careful attention, there are two distinct scenarios that prevent FIS triggering. First, if the shear force is too low or absent, the shear-frictional contribution responsible for ST is too low or null; therefore, there is no transition. Second, if the social force contribution is absent, the dynamics is pure of frictional contact type and, similarly to a gravity-driven granular system when neither external perturbations nor long-range interactions are involved, neither FIS nor DST is observed. For this reason, a combined presence of social force and a large contribution of the shear force are needed to produce the frictionless(social)-friction transition and obtain FIS.

The rheological analysis confirms the previous discussion through the results displayed in Fig. 5b. In this plot, only the cases coinciding with FIS emergence prove to have an abrupt increase in viscosity. An effect that is enhanced when the ratio of shear forces with respect to normal forces is higher. Moreover, this suggests that an exaggerated increment of $\dot{\gamma}$ in front

of the normal force can cause the system to jam or a more pronounced discontinuous shear thickening.

Discussion

The aim of the present research was to establish connections between the concepts of shear thickening and faster-is-slower phenomena. The geometry selected in order to assess this objective was the pedestrian egress from a room through a bottleneck. The work was done through particle-based simulations, concretely using the Social Force Model, and a particular type of boundary conditions was introduced in order to maintain a constant flow rate during the crowd evacuation. To assess the rheological response of the pedestrian crowd, an approach able to compute the relevant magnitudes in generic flows was employed.

The study has confirmed the presence of FIS in pedestrian evacuation despite the introduction of specific boundary conditions that ensure a constant number of particles during the simulation. Based on the time- and spatial-averaged values of area fraction and velocity, we have obtained FIS transition occurrence obeys changes in velocity rather than density since velocity depicted a non-monotonic behavior as a function of the desired velocity. This non-monotonic velocity profile behavior offered the first hint regarding a possible change in the system rheology. Conversely, the area fraction increased monotonically with the increase of v^0 , showing two different rates of increment that corresponded with the maximum velocity and the optimal evacuation time. The increase in area fraction triggers the second FIF domain since the velocity trend is less variable in this range of desired velocities ($v^0 > 5$).

The analysis of the contributions of the social (frictionless) and frictional contact forces to the total stress showed that the frictional shear contact stress overcomes the social contribution. This crossover is also evidence that the crowd rheology presents a complex behavior similar to (non)Brownian suspensions, where this crossover indicates the transition from frictionless to frictional contacts characterized by an onset stress. Supporting this line of reasoning, the found friction coefficient dependency on the desired velocity is in good agreement with this crossover, presenting a maximum value close to the v^0 value that corresponds with the fastest evacuation. In addition, the time- and spatial-averaged shear rate showed an S-shape dependency with the increase of v^0 and, consequently, with the pressure. This is a hallmark of discontinuous shear thickening (DST). This outcome stresses that the local shear rate $\dot{\gamma}$ behaves differently depending on v^0 or P values, transiting from $d\dot{\gamma}/dP > 0$ to $d\dot{\gamma}/dP < 0$. This transition is linked to a change in the system rheology and is, again, a fingerprint of DST. Also, by mapping the viscosity against the total pressure in a zone beyond the exit vicinity, we also demonstrated that DST transition is evident in the bulk in addition to the constriction. This observation, together with the contact network analysis we performed, indicates that a transition from a flowing state to a solid-like state (shear jamming or fragile) is responsible for the DST transition.

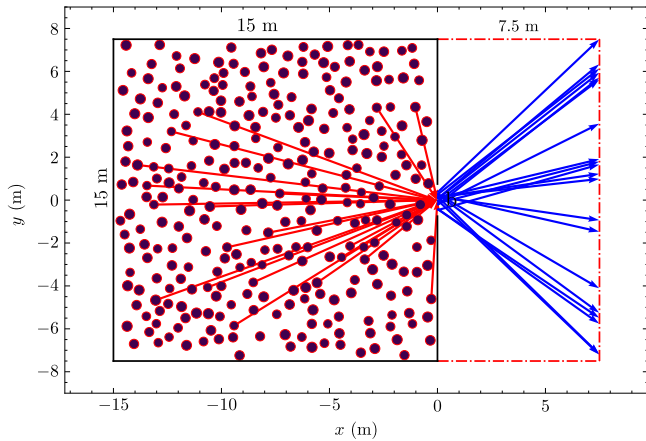


Fig. 6 | Numerical sketch. An example of a typical initial configuration of the $N = 300$ polydispersed pedestrians randomly located in a $15\text{ m} \times 15\text{ m}$ room with an exit of width $b = 3.0D_m$. A random selection of 20 desired velocities in the evacuation room and the same for the second room, pictured with red and blue arrows, respectively. In the evacuation room, desired velocities are vectors pointing from particle positions to the center of the exit, whereas in the second room, the desired velocities point to a random position at the discontinuous vertical line. The employed parameters are $\tau = 0.5\text{ s}$, $A = 2 \times 10^3\text{ N}$, $B = 0.08\text{ m}$, $H = 1.2 \times 10^5\text{ kg s}^{-2}$, and $\gamma = 2.4 \times 10^5\text{ kg m}^{-1}\text{ s}^{-1}$.

Stepping forward, the results for the viscosity of the crowd flow near the exit showed a steep increase at the same point where FIS occurs. This is a clear correlation between the occurrence of FIS and shear thickening. Moreover, the exponential increase of $\eta(P \sim v^0)$ indicates DST materializes with an exponent $\beta = 3$, which implies a multivalued dependency $\eta(\dot{\gamma})$, assuming $\dot{\gamma} \sim P/\eta$ (the inset of Fig. 4a confirms that dependency), highlighting the existence of DST. Also, existing phenomenological theories describe the fraction of frictional contacts $f(v^0)$ as a function of the desired velocity v^0 . These results can be exploited in future contributions to model pedestrian systems using the complex fluid models of the WC type, identifying as a potential candidate the scalar WC model posed recently³⁶. A performed scaling analysis based on refs. 62,63 evidenced the existence of two distinct critical points that determine evacuation crowd dynamics, analogous to the DST transition with two distinct jamming criticalities.

Finally, we have disentangled the influence of the distinct forces in FIS. The results demonstrated that a combined presence of social force and a large contribution of the shear force is required in order to trigger the frictionless(social)-friction transition that leads to FIS. The contact forces cannot activate FIS alone, and a social force interaction is necessary to avoid contacts at low desired speeds. This also suggests that (non)Brownian suspension systems can be more suitable to mimic pedestrian dynamics than classical dry granular systems.

Overall, the obtained results are of double significance. On one side, confirming the correspondence between FIS and shear thickening can be exploited to simulate or describe pedestrian dynamics using complex fluids models and theories stemming from the rheology of suspensions' area. Moreover, equivalent experimental setups embodying (non)Brownian suspensions can shed new light and revisit pedestrian dynamics from a new rheological perspective. This idea is based on the different complexity that presents (non)Brownian suspensions compared to dry granular systems due to the role played by the repulsive(frictionless) force.

Methods

Velocity and position Integration using social force model

The model employed to simulate the pedestrians' evacuation through a bottleneck is the popular social force model (SFM), proposed by Helbing and Molnár in 1995⁶. The SFM is based on Newton's second law and considers three forces to reproduce basic aspects related to the behavior of pedestrians, which were discussed in the section "Introduction". The

velocities and positions of each particle i are obtained by integrating Newton's second law, including all the forces acting on the particle i

$$m_i \frac{dv_i}{dt} = f_i^d + \sum_j (f_{ij}^c + f_{ij}^s). \quad (10)$$

In this work, we integrate Eq. (10) numerically using the Velocity-Störmer-Verlet scheme⁶⁶.

Numerical setup: room scape scenario

In our simulations, we emulate the pedestrians' shapes as circles of diameter uniformly distributed in the range $D_i = [0.45, 0.55]\text{ m}$, resulting in a mean value for the pedestrian diameter $D_m = 0.50\text{ m}$. Initially, $N = 300$ polydispersed pedestrians of mass $m_i = 80\text{ kg}$ are randomly located in a $15\text{ m} \times 15\text{ m}$ room with an exit centered at the middle of the right wall. Figure 6 depicts this room through the black lines. Moreover, we perform simulations for several widths of the exit b , with b ranging from $b = D_m$ to $b = 5D_m$ at intervals of $\Delta b = D_m/2$. The upper bound of the desired velocity of the pedestrians v^0 are evaluated in each run, going from $v^0 = D_m/s$ to $v^0 = 20D_m/s$ at intervals of $\Delta v^0 = D_m/s$. When pedestrians move throughout the room, the desired direction of movement always points to the center of the exit for all the pedestrians, independent of their positions. For $b = \{2D_m, 3D_m\}$, additional desired velocities are considered, which are selected from $v^0 = 0.25D_m/s$ to $v^0 = 3D_m/s$ every $0.25D_m/s$.

It is well known from the literature^{9,15} and also evidenced in our simulations that the evacuation flux is affected by the remaining number of pedestrians left in the room. This result is observed through a change in the slope of the number of pedestrians exiting the outlet as the time increases and prevents obtaining a steady or quasi-steady regime during the whole process. Therefore, in order to keep a constant number of pedestrians in the system and, as a result, to avoid the transient effect, a specific boundary condition is imposed. Namely, a pedestrian that exits the room through the outlet enters a second room with the size $7.5\text{ m} \times 15\text{ m}$, reassigning the desired velocity and pointing towards a random position at the right extreme of the domain. Afterward, the typical periodic boundary conditions are considered. Fig. 6 denotes this second spot with the discontinuous red lines.

Regarding the model's parameters, in the first part of this study, we use the same values employed by Helbing et al. to reproduce the distance kept at characteristic desired velocities and the measured flows through bottlenecks¹. With this aim, the parameters are set as $\tau = 0.5\text{ s}$, $A = 2 \times 10^3\text{ N}$, $B = 0.08\text{ m}$, $H = 1.2 \times 10^5\text{ kg s}^{-2}$, and $\gamma = 2.4 \times 10^5\text{ kg m}^{-1}\text{ s}^{-1}$. Nonetheless, we assess the influence of each force involved in the SFM by evaluating different parameters H , γ , and A . We also isolate the effect of individual interactions by deactivating one or two of the others, thereby allowing the systematic evaluation of the minimum set of ingredients necessary for the FIS phenomenon. As an example, it will explore whether FIS can be reproduced by just maintaining either contact or social forces solely. The used sets of parameters are $f^{s1}, f^{B1,s2}, f^{B1,s1}, f^{B1,S1,s1}, f^{B1,S1}, f^{B1,S2,s1}, f^{S1,s1}$, where f^B , f^s , and f^s denote the body compression, shear, and social forces. In our notation, the superscript stands for activated forces, whilst missing superscripts denote that the force is deactivated. The numbers 1 and 2 designate different numerical values for those interactions in which two different numeric values distinct from zero are explored, with 1 always defining the corresponding parameter already mentioned in the caption of Fig. 6. For the frictional force case f^s , 2 stands for the additional friction parameter $\gamma = 2.4 \times 10^4\text{ kg m}^{-1}\text{ s}^{-1}$. Similarly, for the social force label (f^s), we selected a supplementary $A = 3.2 \times 10^3\text{ N}$ value and represented by 2. The other parameters remain invariable. For example, the case $f^{SB1,s2}$ means that the shear force is deactivated, contrary to the body compression and social forces that are activated. Moreover, for this case, all the values for the

simulation are as those mentioned in the caption of Fig. 6 except the parameter A , which is $A = 3.2 \times 10^3 \text{ N}$ due to the 2 accompanying the superscript for the social force. The total time for each simulation is fixed at 1000 s with a numerical time step chosen to be $\Delta t = 10^{-3} \text{ s}$.

Coarse-graining (CG) micro-macro mapping

To examine the results of the numerical simulations and to facilitate insight into the complex behavior of the considered system, we have employed coarse-graining mapping. In this way, the microscopic magnitudes provided by the simulations, such as positions, velocities, and interaction forces, are mapped into macroscopic fields. To carry out this task, CG requires introducing a non-negative integrable function $\varphi_i(\mathbf{r})$. Here, a truncated Gaussian function $\varphi(\mathbf{r}) = A_\omega^{-1} \exp[-(\mathbf{r} - \mathbf{r}_i)^2 / 2\omega^2]$ is selected with $\omega = D_m/2$, where A_ω^{-1} is the normalization constant such that $\varphi_i(\mathbf{r})$ is normalized in the interval $[-r_c, r_c]$, being $r_c = 3\omega$ the cut-off length. Thus, the macroscopic mean fields of density $\rho(\mathbf{r}, t)$, momentum $\mathbf{P}(\mathbf{r}, t)$, and velocity $\mathbf{V}(\mathbf{r}, t) = \mathbf{P}(\mathbf{r}, t) / \rho(\mathbf{r}, t)$ are obtained from the particle positions \mathbf{r}_i and velocities \mathbf{v}_i , respectively. Complementarily, the components of the shear rate tensor $\dot{\gamma}^{\alpha\beta}$ are numerically computed via central difference.

The stress field $\boldsymbol{\sigma}(\mathbf{r}, t)$ is computed using the formulation introduced in refs. 67,68. Following this approach, the stress $\boldsymbol{\sigma}(\mathbf{r}, t) = \boldsymbol{\sigma}^k(\mathbf{r}, t) + \boldsymbol{\sigma}^f(\mathbf{r}, t)$ has two contributions: the kinetic stress field $\boldsymbol{\sigma}^k(\mathbf{r}, t)$ and an interaction-force stress field $\boldsymbol{\sigma}^f(\mathbf{r}, t) = \boldsymbol{\sigma}^c(\mathbf{r}, t) + \boldsymbol{\sigma}^s(\mathbf{r}, t)$, with superscripts c and s denoting the contact and social contributions, respectively.

The interaction-force stress field $\boldsymbol{\sigma}^f(\mathbf{r}, t)$ is computed from the interaction forces and branch vectors \mathbf{r}_{ij} by the line integral of $\varphi(\mathbf{r})$ along \mathbf{r}_{ij} as follows:

$$\boldsymbol{\sigma}^f(\mathbf{r}, t) = \sum_{i=1}^N \sum_{j=1}^{N_c} \mathbf{r}_{ij} \otimes \mathbf{F}_{ij} \int_0^1 \varphi(\mathbf{r} - \mathbf{r}_i + s\mathbf{r}_{ij}) ds. \quad (11)$$

On the other hand, the kinetic stress $\boldsymbol{\sigma}^k(\mathbf{r}, t)$ accounts for the velocity fluctuations relative to the mean velocity field $\mathbf{V}(\mathbf{r}, t)$. Defining the fluctuations of the velocity as $\mathbf{v}'_i = \mathbf{v}_i - \mathbf{V}(\mathbf{r}, t)$, the kinetic stress yields

$$\boldsymbol{\sigma}^k(\mathbf{r}, t) = \sum_{i=1}^N \mathbf{v}'_i \otimes \mathbf{v}'_i \varphi_i. \quad (12)$$

in the framework of the coarse-graining methodology.

Based on the previous formulation, a post-processing data analysis tool was implemented. It allows the computation of all the relevant macroscopic fields using the SFM simulations' outcomes as input data.

Rheology from complex flows

Standard rheological characterization of complex fluids is usually done under viscometric flows⁶⁹. Giusteri and Seto recently introduced a general decomposition of the stress tensor for incompressible fluids in generic flow conditions⁷⁰. In their proposed framework, the velocity gradient $\nabla \mathbf{u}$ is expressed in terms of its symmetric \mathbf{D} and antisymmetric \mathbf{W} part as follows:

$$\nabla \mathbf{u} = \mathbf{D} + \mathbf{W} \quad (13)$$

Employing this decomposition of the velocity gradient and expressing \mathbf{D} and \mathbf{W} in the base of the unit-norm eigenvectors of \mathbf{D} , a generalized system viscosity η is inferred to hold the following form

$$\eta = \frac{1}{2} \frac{\boldsymbol{\sigma} : \mathbf{D}}{\mathbf{D} : \mathbf{D}} \quad (14)$$

under steady simple shear flow, η becomes exactly the shear viscosity. $\boldsymbol{\sigma} = \boldsymbol{\sigma}^k + \boldsymbol{\sigma}^c + \boldsymbol{\sigma}^f$ is the total stress. It can be split into normal and shear contributions, $\boldsymbol{\sigma} = \text{Tr}(\boldsymbol{\sigma})\mathbb{1} + \boldsymbol{\tau}$. The normal contribution can be rationalized in terms of the hydrodynamic pressure (first tensor invariant) $P = \text{Tr}(\boldsymbol{\sigma})/2$. In contrast, the shear contribution can be quantified through

the second invariant of $\boldsymbol{\sigma}$, $\tau = 1/2\sqrt{(\lambda_1 - \lambda_2)^2}$, where λ_1 and λ_2 are the eigenvalues of the stress tensor.

Moreover, a measure of macroscopic friction can be quantified as tensor-invariant finding the deviatoric stress relative to pressure, which reads

$$\mu^c = \frac{\sqrt{(\lambda_1^c - \lambda_2^c)^2}}{\sqrt{6}p^c}, \quad (15)$$

where λ_1^c and λ_2^c are the eigenvalues of the contact stress tensor $\boldsymbol{\sigma}^c$, whereas p^c is the contact pressure which is $\text{Tr}(\boldsymbol{\sigma}^c)/2$. When the strain rate and stress are collinear, this quantity is precisely the Coulomb coefficient of friction.

Data availability

Those interested in requesting the data related to this contribution can contact the corresponding authors. The data can also be easily obtained using the code, which is available at https://github.com/BCAM-CFD/evacuation_pedestrians.

Code availability

The code can be found at https://github.com/BCAM-CFD/evacuation_pedestrians.

Received: 30 August 2023; Accepted: 26 April 2024;

Published online: 10 May 2024

References

- Helbing, D., Farkas, I. & Vicsek, T. Simulating dynamical features of escape panic. *Nature* **407**, 487–490 (2000).
- Haghani, M. Empirical methods in pedestrian, crowd and evacuation dynamics: Part I. Experimental methods and emerging topics. *Saf. Sci.* **129**, 104743 (2020).
- Shiwakoti, N., Shi, X. & Ye, Z. A review on the performance of an obstacle near an exit on pedestrian crowd evacuation. *Saf. Sci.* **113**, 54–67 (2019).
- Garcimartín, A. et al. Redefining the role of obstacles in pedestrian evacuation. *N. J. Phys.* **20**, 123025 (2018).
- Shi, X., Ye, Z., Shiwakoti, N., Tang, D. & Lin, J. Examining effect of architectural adjustment on pedestrian crowd flow at bottleneck. *Physica A* **522**, 350–364 (2019).
- Helbing, D. & Molnár, P. Social force model for pedestrian dynamics. *Phys. Rev. E* **51**, 4282 (1995).
- Garcimartín, A., Zuriguel, I., Pastor, J., Martín-Gómez, C. & Parisi, D. Experimental evidence of the “faster is slower” effect. *Transp. Res. Procedia* **2**, 760–767 (2014).
- Pastor, J. M. et al. Experimental proof of faster-is-slower in systems of frictional particles flowing through constrictions. *Phys. Rev. E* **92**, 062817 (2015).
- Garcimartín, A., Parisi, D. R., Pastor, J. M., Martín-Gómez, C. & Zuriguel, I. Flow of pedestrians through narrow doors with different competitiveness. *J. Stat. Mech.: Theory Exp.* **2016**, 043402 (2016).
- Hidalgo, R., Parisi, D. R. & Zuriguel, I. Simulating competitive egress of noncircular pedestrians. *Phys. Rev. E* **95**, 042319 (2017).
- García, A. et al. Analysis of local density during football stadium access: Integrating pedestrian flow simulations and empirical data. *Physica A* **638**, 129635 (2024).
- Johansson, A., Helbing, D. & Shukla, P. K. Specification of the social force pedestrian model by evolutionary adjustment to video tracking data. *Adv. Complex Syst.* **10**, 271–288 (2007).
- Zanlungo, F., Ikeda, T. & Kanda, T. Social force model with explicit collision prediction. *Europhys. Lett.* **93**, 68005 (2011).
- García, A., Hernández-Delfin, D., Lee, D.-J. & Ellero, M. Limited visual range in the social force model: effects on macroscopic and microscopic dynamics. *Physica A* **612**, 128461 (2023).

15. Parisi, D. R. & Dorso, C. O. Microscopic dynamics of pedestrian evacuation. *Physica A* **354**, 606–618 (2005).
16. Parisi, D. R. & Dorso, C. O. Morphological and dynamical aspects of the room evacuation process. *Physica A* **385**, 343–355 (2007).
17. Arévalo, R., Zuriguel, I., Maza, D. & Garcimartín, A. Role of driving force on the clogging of inert particles in a bottleneck. *Phys. Rev. E* **89**, 042205 (2014).
18. Gago, P. A., Parisi, D. R. & Pugnaloni, L. A. “Faster is slower” effect in granular flows. In *Traffic and Granular Flow'11* (eds Kozlov, V. et al.) 317–324 (Springer, 2013).
19. Echeverría-Huarte, I., Zuriguel, I. & Hidalgo, R. C. Pedestrian evacuation simulation in the presence of an obstacle using self-propelled spherocylinders. *Phys. Rev. E* **102**, 012907 (2020).
20. Cornes, F. E., Frank, G. A. & Dorso, C. O. Microscopic dynamics of the evacuation phenomena in the context of the social force model. *Physica A* **568**, 125744 (2021).
21. Seto, R., Mari, R., Morris, J. F. & Denn, M. M. Discontinuous shear thickening of frictional hard-sphere suspensions. *Phys. Rev. Lett.* **111**, 218301 (2013).
22. Mari, R., Seto, R., Morris, J. F. & Denn, M. M. Shear thickening, frictionless and frictional rheologies in non-brownian suspensions. *J. Rheol.* **58**, 1693–1724 (2014).
23. Maiti, M., Zippelius, A. & Heussinger, C. Friction-induced shear thickening: a microscopic perspective. *Europhys. Lett.* **115**, 54006 (2016).
24. Hoffman, R. Discontinuous and dilatant viscosity behavior in concentrated suspensions. I. Observation of a flow instability. *Trans. Soc. Rheol.* **16**, 155–173 (1972).
25. Hoffman, R. Discontinuous and dilatant viscosity behavior in concentrated suspensions. II. Theory and experimental tests. *J. Colloid Interface Sci.* **46**, 491–506 (1974).
26. Barnes, H. Shear-thickening (“dilatancy”) in suspensions of nonaggregating solid particles dispersed in Newtonian liquids. *J. Rheol.* **33**, 329–366 (1989).
27. Wagner, N. J. & Brady, J. F. Shear thickening in colloidal dispersions. *Phys. Today* **62**, 27–32 (2009).
28. Bian, X., Litvinov, S., Ellero, M. & Wagner, N. J. Hydrodynamic shear thickening of particulate suspension under confinement. *J. Non-Newton. Fluid Mech.* **213**, 39–49 (2014).
29. Brown, E. & Jaeger, H. M. Shear thickening in concentrated suspensions: phenomenology, mechanisms and relations to jamming. *Rep. Prog. Phys.* **77**, 046602 (2014).
30. Wyart, M. & Cates, M. E. Discontinuous shear thickening without inertia in dense non-Brownian suspensions. *Phys. Rev. Lett.* **112**, 098302 (2014).
31. Guy, B., Hermes, M. & Poon, W. C. Towards a unified description of the rheology of hard-particle suspensions. *Phys. Rev. Lett.* **115**, 088304 (2015).
32. Morris, J. F. Shear thickening of concentrated suspensions: recent developments and relation to other phenomena. *Annu. Rev. Fluid Mech.* **52**, 121–144 (2020).
33. Singh, A., Ness, C., Seto, R., de Pablo, J. J. & Jaeger, H. M. Shear thickening and jamming of dense suspensions: the “roll” of friction. *Phys. Rev. Lett.* **124**, 248005 (2020).
34. Hsu, C.-P., Mandal, J., Ramakrishna, S. N., Spencer, N. D. & Isa, L. Exploring the roles of roughness, friction and adhesion in discontinuous shear thickening by means of thermo-responsive particles. *Nat. Commun.* **12**, 1477 (2021).
35. Vázquez-Quesada, A., Wagner, N. & Ellero, M. Planar channel flow of a discontinuous shear-thickening model fluid: theory and simulation. *Phys. Fluids* **29**, 103104 (2017).
36. Angerman, P., Prasanna Kumar, S. S., Seto, R., Sandnes, B. & Ellero, M. Microstructural smoothed particle hydrodynamics model and simulations of discontinuous shear-thickening fluids. *Phys. Fluids* **36**, 033103 (2024).
37. Gillissen, J. J., Ness, C., Peterson, J. D., Wilson, H. J. & Cates, M. E. Constitutive model for time-dependent flows of shear-thickening suspensions. *Phys. Rev. Lett.* **123**, 214504 (2019).
38. Singh, A., Mari, R., Denn, M. M. & Morris, J. F. A constitutive model for simple shear of dense frictional suspensions. *J. Rheol.* **62**, 457–468 (2018).
39. Baumgarten, A. S. & Kamrin, K. A general constitutive model for dense, fine-particle suspensions validated in many geometries. *Proc. Natl Acad. Sci. USA* **116**, 20828–20836 (2019).
40. Krieger, I. M. & Dougherty, T. J. A mechanism for non-newtonian flow in suspensions of rigid spheres. *Trans. Soc. Rheol.* **3**, 137–152 (1959).
41. Behringer, R. P. & Chakraborty, B. The physics of jamming for granular materials: a review. *Rep. Prog. Phys.* **82**, 012601 (2018).
42. Zhao, Y. et al. Shear-jammed, fragile, and steady states in homogeneously strained granular materials. *Phys. Rev. Lett.* **123**, 158001 (2019).
43. Thomas, J. E. et al. Microscopic origin of frictional rheology in dense suspensions: correlations in force space. *Phys. Rev. Lett.* **121**, 128002 (2018).
44. Hermes, M. et al. Unsteady flow and particle migration in dense, non-brownian suspensions. *J. Rheol.* **60**, 905–916 (2016).
45. Zuriguel, I. et al. Clogging transition of many-particle systems flowing through bottlenecks. *Sci. Rep.* **4**, 7324 (2014).
46. Zuriguel, I. & Garcimartín, A. *Statistical Mechanics of Clogging* 1–32 (Springer, Berlin, Heidelberg, 2020).
47. Liu, A. J. & Nagel, S. R. Jamming is not just cool any more. *Nature* **396**, 21–22 (1998).
48. Sarkar, S., Bi, D., Zhang, J., Behringer, R. & Chakraborty, B. Origin of rigidity in dry granular solids. *Phys. Rev. Lett.* **111**, 068301 (2013).
49. Goyal, A., Martys, N. S. & Del Gado, E. Flow induced rigidity percolation in shear thickening suspensions. *J. Rheol.* **68**, 219–228 (2024).
50. Cates, M., Wittmer, J., Bouchaud, J.-P. & Claudin, P. Jamming, force chains, and fragile matter. *Phys. Rev. Lett.* **81**, 1841 (1998).
51. Bi, D., Zhang, J., Chakraborty, B. & Behringer, R. P. Jamming by shear. *Nature* **480**, 355–358 (2011).
52. Pan, D., Wang, Y., Yoshino, H., Zhang, J. & Jin, Y. A review on shear jamming. *Phys. Rep.* **1038**, 1–18 (2023).
53. Otsuki, M. & Hayakawa, H. Shear jamming, discontinuous shear thickening, and fragile states in dry granular materials under oscillatory shear. *Phys. Rev. E* **101**, 032905 (2020).
54. Seto, R., Singh, A., Chakraborty, B., Denn, M. M. & Morris, J. F. Shear jamming and fragility in dense suspensions. *Granul. Matter* **21**, 1–8 (2019).
55. Péter, H., Libál, A., Reichhardt, C. & Reichhardt, C. O. Crossover from jamming to clogging behaviours in heterogeneous environments. *Sci. Rep.* **8**, 10252 (2018).
56. Stoop, R. L. & Tierno, P. Clogging and jamming of colloidal monolayers driven across disordered landscapes. *Commun. Phys.* **1**, 68 (2018).
57. López, D., Hernández-Delfin, D., Hidalgo, R. C., Maza, D. & Zuriguel, I. Clogging-jamming connection in narrow vertical pipes. *Phys. Rev. E* **102**, 010902 (2020).
58. Ramola, K. & Chakraborty, B. Stress response of granular systems. *J. Stat. Phys.* **169**, 1–17 (2017).
59. Souzy, M. & Marin, A. Role of liquid driving on the clogging of constricted particle suspensions. *J. Fluid Mech.* **953**, A40 (2022).
60. Ozturk, D., Morgan, M. L. & Sandnes, B. Flow-to-fracture transition and pattern formation in a discontinuous shear thickening fluid. *Commun. Phys.* **3**, 119 (2020).
61. Ruiz-Lopez, J. A., Prasanna Kumar, S. S., Vazquez-Quesada, A., de Vicente, J. & Ellero, M. Tribological variable-friction coefficient models for the simulation of dense suspensions of rough polydisperse particles. *J. Rheol.* **67**, 541–558 (2023).
62. Ramaswamy, M. et al. Universal scaling of shear thickening transitions. *J. Rheol.* **67**, 1189–1197 (2023).

63. Malbranche, N., Santra, A., Chakraborty, B. & Morris, J. F. Scaling analysis of shear thickening suspensions. *Front. Phys.* **10**, 946221 (2022).
64. Cardy, J. *Scaling, and Renormalization in Statistical Physics* Vol. 5 (Cambridge University Press, 1996).
65. Sticco, I. M., Frank, G. A. & Dorso, C. O. Effects of the body force on the pedestrian and the evacuation dynamics. *Saf. Sci.* **129**, 104829 (2020).
66. Hairer, E., Lubich, C. & Wanner, G. Geometric numerical integration illustrated by the Störmer–Verlet method. *Acta Numer.* **12**, 399–450 (2003).
67. Babic, M. Average balance equations for granular materials. *Int. J. Eng. Sci.* **35**, 523–548 (1997).
68. Goldhirsch, I. Stress, stress asymmetry and couple stress: from discrete particles to continuous fields. *Granul. Matter* **12**, 239 (2010).
69. Bird, R. B., Armstrong, R. C. & Hassager, O. *Dynamics of Polymeric Liquids* Vol. 1: *Fluid Mechanics* (John Wiley and Sons Inc., New York, NY, 1987).
70. Giusteri, G. G. & Seto, R. A theoretical framework for steady-state rheometry in generic flow conditions. *J. Rheol.* **62**, 713–723 (2018).

Acknowledgements

This research is supported by the Basque Government through the BERG 2022–2025 program and by the Spanish Government (AEI/FEDER) through BCAM Severo Ochoa excellence accreditation CEX2021-001142-S/MICIN/AEI/10.13039/501100011033. The authors also acknowledge the financial support received by the Basque Government through the “Mathematical Modeling Applied to Health” Project and the Diputación Foral de Bizkaia through the “M³OVE” Project. The authors sincerely appreciate the suggestions and comments of the anonymous reviewers, which contributed to improving the manuscript’s quality.

Author contributions

D.H. conceived and conducted the simulations. A.G., M.E., and D.H. analyzed the results and reviewed the manuscript.

Competing interests

The authors declare no competing interests.

Additional information

Supplementary information The online version contains supplementary material available at <https://doi.org/10.1038/s42005-024-01646-1>.

Correspondence and requests for materials should be addressed to Dariel Hernández-Delfin or Marco Ellero.

Peer review information *Communications Physics* thanks the anonymous reviewers for their contribution to the peer review of this work. A peer review file is available.

Reprints and permissions information is available at <http://www.nature.com/reprints>

Publisher’s note Springer Nature remains neutral with regard to jurisdictional claims in published maps and institutional affiliations.

Open Access This article is licensed under a Creative Commons Attribution 4.0 International License, which permits use, sharing, adaptation, distribution and reproduction in any medium or format, as long as you give appropriate credit to the original author(s) and the source, provide a link to the Creative Commons licence, and indicate if changes were made. The images or other third party material in this article are included in the article’s Creative Commons licence, unless indicated otherwise in a credit line to the material. If material is not included in the article’s Creative Commons licence and your intended use is not permitted by statutory regulation or exceeds the permitted use, you will need to obtain permission directly from the copyright holder. To view a copy of this licence, visit <http://creativecommons.org/licenses/by/4.0/>.

© The Author(s) 2024